

## Quantum paraelectricity of BaFe<sub>12</sub>O<sub>19</sub>

Xuefeng Zhang <sup>1</sup>, Qi-Jun Ye,<sup>1,\*</sup> Hongjun Xiang,<sup>2</sup> and Xin-Zheng Li <sup>1,3,†</sup>

<sup>1</sup>State Key Laboratory for Artificial Microstructure and Mesoscopic Physics, Frontier Science Center for Nano-optoelectronics and School of Physics, Peking University, Beijing 100871, People's Republic of China

<sup>2</sup>Key Laboratory of Computational Physical Sciences (Ministry of Education), State Key Laboratory of Surface Physics, and Department of Physics, Fudan University, Shanghai 200433, People's Republic of China

<sup>3</sup>Collaborative Innovation Center of Quantum Matter, Peking University, Beijing 100871, People's Republic of China



(Received 27 January 2020; accepted 27 February 2020; published 18 March 2020)

Using path-integral Monte Carlo sampling and a lattice Wannier function based effective Hamiltonian obtained from first principles, we show that the quantum fluctuations of the nuclei play a central role in the paraelectric phase of BaFe<sub>12</sub>O<sub>19</sub> at low temperatures ( $T$ 's). Contribution from the geometrical frustrations, on the other hand, is negligible. The  $T$  dependence of the dielectric function and the displacements of the Fe ions reported in previous experiments were reproduced. The nature of the quantum paraelectrics (QPEs) was assigned to order-disorder or displacive, using the relative magnitudes of the on-site/intersite energies of the electric dipoles, and the quantum fluctuations of the nuclei in the path-integral samplings. This study provides a unified atomic-level picture of QPEs, which could be used to understand different experiments in which new QPE materials were found.

DOI: [10.1103/PhysRevB.101.104102](https://doi.org/10.1103/PhysRevB.101.104102)

### I. INTRODUCTION

The quantum paraelectric (QPE) phase is a state of matter in which the long-range order of the electric dipoles, induced by the mechanical instability of its high-symmetry phase, is prevented by the quantum fluctuations of the nuclei when the temperature ( $T$ ) approaches 0 K [1]. It is a phenomenon that is qualitatively different from the conventional paraelectric (PE) phase, which undergoes a PE to ferroelectric (FE) phase transition upon cooling, when the thermal fluctuations of the nuclei cannot resist the long-range ordering of the electric dipoles. As a result, the PE-FE phase transition is absent in QPEs and the dielectric constant becomes independent of  $T$  at low  $T$ 's.

Since the first experimental discovery of QPEs in SrTiO<sub>3</sub> [2], discussions about their properties, such as the dielectric constant, the structural phase transitions, and their interactions with electronic correlation effects, have continued [1,3–6]. But in comparison with other quantum phases of matter, e.g. superconductors, such follow-up studies are very rare, mainly due to the lack of examples.

Recently, M-type hexaferrite BaFe<sub>12</sub>O<sub>19</sub> has received much research attention because of its nontrivial electric and magnetic polarization behaviors [7–11]. Since its discovery in the 1950s, this material has been commercially and technologically important due to its ferrimagnetic properties [7,12].

According to space group symmetry ( $P6_3/mmc$ ), it has a magnetoplumbite-type structure with Fe ions located in the Fe-O tetrahedral (TET), octahedral (OCT), and trigonal bipyramidal (TBP) sites [Fig. 1(a)]. Many experiments, how-

ever, including those on the Mössbauer spectrum [13,14], x-ray diffraction [15], and neutron diffraction [8,16], show noticeable displacements of Fe ions in the Fe-O TBP site from the center of the mirror plane of the TBP site (2b site) to the two adjacent tetrahedral sites (4e site) located along the  $c$ -axis, as shown in Fig. 1(a).

To address this puzzle, Wang *et al.* calculated the displacements of Fe ions in the TBP sites along  $z$  using first-principles geometry optimizations in 2014, and they predicted that it could be a multiferroic material with the possible coexistence of a ferrimagnet and antiferroelectricity (AFE) [9].

Recent experiments, however, have shown that the dielectric constants are saturated at low- $T$ 's [10], and the long-range-ordered AFE state is absent. Inspired by the triangular nature of the BaFe<sub>12</sub>O<sub>19</sub> layer, in a subsequent paper of Ref. [10], Shen *et al.* proposed that BaFe<sub>12</sub>O<sub>19</sub> is possibly a quantum electric-dipole liquid, and geometrical frustrations of the AFE coupling play a central role in inducing this nontrivial state [11].

The AFE coupling of this material, however, is very different from the conventional anti-parallel coupling between neighboring sites in the geometrically frustrated quantum systems. The saturation of the dielectric constant at low  $T$  also shares a strong similarity to QPEs. Therefore, theoretical simulations at finite  $T$  are needed to clarify the atomic-level details of what is happening in this material upon cooling. To the best of our knowledge, such a theoretical study has not been done yet due to some challenges to standard methods. For example, very large supercells are needed to properly describe the long-range interactions between polarized unit cells and to ensure that the thermodynamic limit is reached, which makes direct *ab initio* simulations impractical.

Static calculation methods (such as geometry optimization) are incapable of addressing the effects of finite- $T$

\*qjye@pku.edu.cn

†xzli@pku.edu.cn

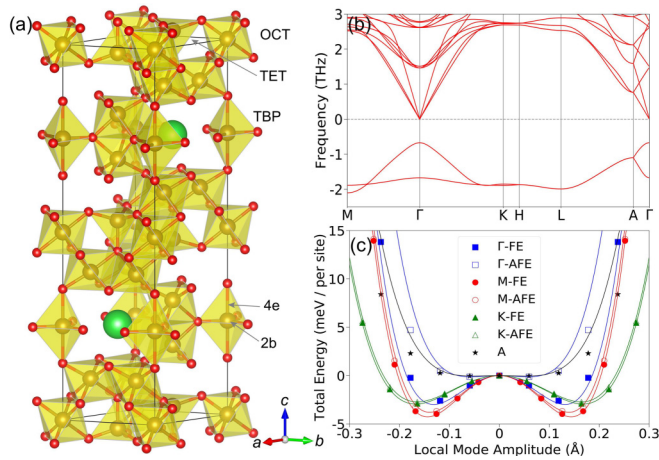


FIG. 1. (a) Crystal structure of  $\text{BaFe}_{12}\text{O}_{19}$ . Green balls denote Ba ions, yellow balls denote Fe ions, and red balls denote O ions. (b) Phonon spectrum of  $\text{BaFe}_{12}\text{O}_{19}$  calculated by the first-principles calculations using PBE+U. (c) A comparison between the potential energy surface (PES) obtained from our model Hamiltonian (solid lines) and from DFT (markers) calculations. PESs along different high-symmetry  $\mathbf{k}$ -points were denoted by different markers, and the results calculated along the same  $\mathbf{k}$ -points by the model and DFT were represented by the same color.

thermal/quantum fluctuations, and Monte Carlo or molecular dynamics with sufficient sampling are needed. When the quantum fluctuations are important, the quantum nature of the nuclei is also important.

In this article, we studied the electric polarization behaviors of  $\text{BaFe}_{12}\text{O}_{19}$  using a combination of the path-integral Monte Carlo (PIMC) method and an effective lattice Hamiltonian method, with the difficulties mentioned above fully accounted for. This Hamiltonian is constructed by a set of local modes called lattice Wannier functions, using a scheme suggested by Íñiguez *et al.* [17], which is numerically as accurate as density-functional theory (DFT) and computationally as efficient as the force-field method. In so doing, we can employ supercells containing tens of thousands of atoms to compute the  $T$  dependence of the dielectric constant and address the competition between the thermal and quantum fluctuations of the nuclei at finite  $T$  in a very clean manner.

Our simulations reproduced the plateau of the dielectric constant versus  $T$  curve, and proved that the quantum fluctuations of the nuclei are responsible for this plateau at low  $T$  in  $\text{BaFe}_{12}\text{O}_{19}$ , meaning that it is a QPE material. The influence of geometry frustration on the dielectric constant, on the other hand, is only of minor importance.

Besides these, we also explained the displacements of Fe ions in the TBP sites observed in experiments such as the Mössbauer spectrum and neutron/x-ray diffractions, as a result of the order-disorder-type nature of this paraelectric material. The on-site energy of the electric dipoles dominates in the energy term of the effective lattice Hamiltonian. Quantum fluctuations of the nuclei can wash out the long-range order of the electric dipoles, but the local moment holds. As such, the crystal possesses a  $P6_3/mmc$  symmetry and a QPE phase at low  $T$  by statistical average, but the distribution of the Fe ions has peaks that deviated from the mirror plane of TBP to

the two adjacent tetrahedral sites ( $4e$  site) located along the  $c$ -axis.

Already in the 1970s, a theoretical analysis on how an ordered ferroelectric phase was suppressed by quantum fluctuations had been given in a cubic ferrodistorive model [18], with a focus on the displacive QPEs. Following a similar idea, we performed a systematic investigation into how QPEs are induced by looking at the relative magnitudes of the onsite/intersite energies of the electric dipoles, and the quantum fluctuations of the nuclei in the path-integral samplings.

Our analysis shows that, like thermal paraelectric, the QPEs can also be classified as of order-disorder or of displacive types, according to the relative magnitudes between the on-site, intersite energies, and quantum fluctuations. This study presents a simple and unified atomic level picture of the QPE properties in  $\text{BaFe}_{12}\text{O}_{19}$ , which could be used to understand different experiments when new QPE materials were found.

This article is organized as follows. In Sec. II, we present the methodology of constructing an effective lattice Hamiltonian for  $\text{BaFe}_{12}\text{O}_{19}$ . The computational details of obtaining the model coefficients and performing the PIMC simulations are also provided. In Sec. III, we discuss the results on the  $T$ -dependence of the dielectric constants and microscopic properties of  $\text{BaFe}_{12}\text{O}_{19}$ , as well as a discussion of how the microscopic properties are influenced by the relationship between on-site energy, inter-site energies of the electric dipoles, and the quantum fluctuations of the nuclei. A summary of the conclusions is given in Sec. IV.

## II. METHODS

### A. Effective Lattice Hamiltonian

#### 1. $\text{BaFe}_{12}\text{O}_{19}$

To generate the effective lattice Hamiltonian for simulating the finite- $T$  FE and PE phases as well as their possible transitions in  $\text{BaFe}_{12}\text{O}_{19}$ , we choose a set of real-space localized basis, called lattice Wannier functions (or local modes). Such a lattice Wannier function was first suggested by Kohn in 1973 [19], written as

$$w_i^{\mathbf{R}_0}[\mathbf{R}_{N,v}, s] = \frac{1}{N} \sum_{\mathbf{k}} e^{i\mathbf{k} \cdot [\mathbf{R}_{N,v} - \mathbf{R}_0]} \left[ \sum_{s'}^n M_{ss'}^{\mathbf{k}} \xi_i^{\mathbf{k}}(v, s') \right]. \quad (1)$$

Here,  $\mathbf{R}_0$  means the position vector of the Wannier function center (WFC),  $\mathbf{R}_{N,v}$  denotes the position vector of the  $v$ th atom in the  $N$ th unit cell,  $s, s'$  are the index of the phonon branches included in the effective lattice Hamiltonian,  $i = x, y, z$  denotes the Cartesian component, and  $\sum_{\mathbf{k}}^{\text{BZ}}$  means the integration of the  $\mathbf{k}$  vector over the first Brillouin zone.  $\xi$  is the phonon eigenvector.  $M^{\mathbf{k}}$  is a linear transformation to make the Wannier functions localized. In the electron case, there is a “gauge freedom” in the electronic Bloch function.

By choosing a good gauge, one can get a set of well-localized Wannier functions [20]. In the lattice case, a few schemes were suggested to make the basis functions localized [17,21,22].

In this study, we follow the scheme suggested by Íñiguez and co-workers [17], which chooses  $M^{\mathbf{k}}$  so that  $\sum_i^n M_{ji}^{\mathbf{k}} \xi_i^{\mathbf{k}}$  at different  $\mathbf{k}$  can add their contribution coherently at the WFC.

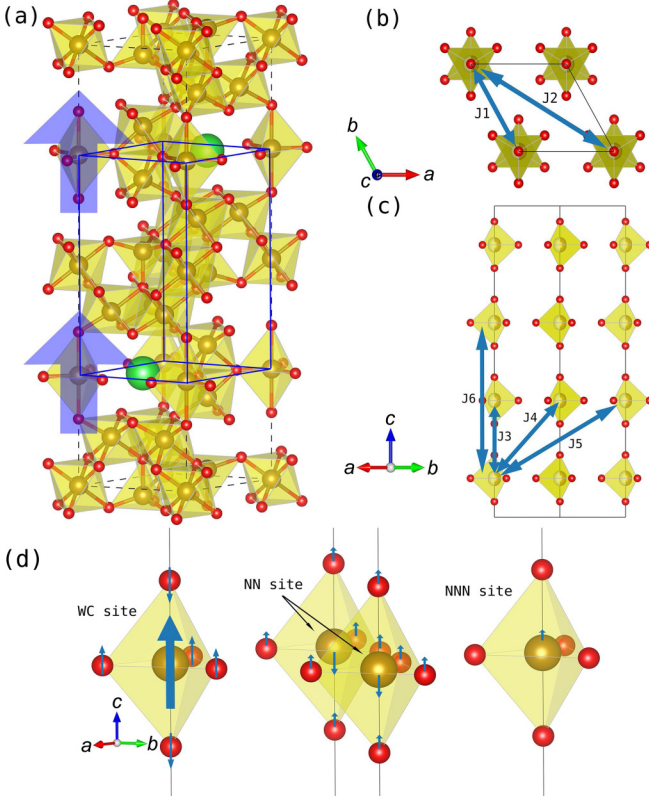


FIG. 2. (a) Schematic of the redefined lattice (blue lines) used in our model. Parts (b) and (c) show the short-range intersite coupling contained in our model. For clarity, we show only the TBP Fe-O polyhedrons whose centers are located on the 2b site (the lattice site of our re-defined lattice). (d) Schematic of the lattice Wannier function.

In so doing the interference effects dampen the amplitude of the displacements at sites away from the WFCs. We choose the WFCs to be located at the Wyckoff positions, which dominate the properties of phonon branches associated with the effective lattice Hamiltonian.

As shown in Fig. 1(b), there are two soft phonon branches in the whole Brillouin zone. Analysis of the phonon eigenvectors show that these soft modes are dominated by the displacements of the Fe ions on the 2b sites along the *c*-axis, in agreement with previous experiments [8, 13–16]. Therefore, we choose the Fe ions on the 2b sites as the WFCs.

We show a schematic of our constructed lattice Wannier function in Fig. 2(d). Only the TBP polyhedrons at the WFC site, the nearest-neighbor (NN), and the next-nearest-neighbor (NNN) sites are shown. The size of arrows reflects the relative magnitude of the lattice Wannier functions.

More than 90% of the weight of the lattice Wannier function is located on the WFC sites, meaning that the lattice Wannier functions are well-localized. Then, the lattice vibrations associated with those two soft phonon branches can be represented by superpositions of all the lattice WFCs at different 2b sites of the crystal. It should be noted that the WFCs at two different 2b sites in one unit cell are equal to each other because of symmetry. Therefore, we can treat them with the same label on a redefined lattice consisting purely of an array of 2b sites [see Fig. 2(a)].

Denoting the amplitude of the lattice Wannier function on site *i* (here we use the re-defined lattice) as  $u_i$ , the effective lattice Hamiltonian can be written as

$$\begin{aligned}
 H(\{u_i\}, \{\eta\}) = & \sum_i (\kappa u_i^2 + \alpha u_i^4) + \sum_{\lambda=1}^6 \sum_{\langle i,j \rangle_\lambda} J_{ij}^\lambda u_i u_j \\
 & + \frac{Z_{\text{eff}}^2}{\epsilon_\infty} \sum_{i<j} \frac{\mathbf{u}_i \cdot \mathbf{u}_j - 3(\hat{\mathbf{R}}_{ij} \cdot \mathbf{u}_i)(\hat{\mathbf{R}}_{ij} \cdot \mathbf{u}_j)}{R_{ij}^3} \\
 & + \sum_i B \eta u_i^2.
 \end{aligned} \quad (2)$$

The first term is the on-site energy, with the quartic contribution included to address anharmonicity. The second and third terms correspond to the intersite couplings. The short-range intersite coupling considered in our model is shown in Figs. 2(b) and 2(c), and the long-range part of the intersite coupling is represented by a classical dipole-dipole interaction.

$Z_{\text{eff}}$  denotes the Born effective charge of the lattice Wannier function, and  $\epsilon_\infty$  denotes the optical dielectric constant, which can be obtained from the first-principles calculations. The fourth term denotes the coupling between the strains (strength is denoted by  $\eta$ ) and the magnitude of soft phonons. It is the only adjustable parameter in this model.

To obtain the coefficients in the above model Hamiltonian, we fit them to the first-principles Born-Oppenheimer potential energy surface (PES) along the soft phonon eigenvectors on the high-symmetry points in the Brillouin zone. The normal modes at  $\Gamma(0, 0, 0)$ ,  $M(0, 1/2, 0)$ ,  $K(1/3, 1/3, 0)$ , and  $A(0, 0, 1/2)$  are used, and all the curves are fitted by quartic functions. The quartic coefficients obtained have similar values, therefore we use their average as  $\alpha$ . The long-range dipole-dipole interactions are calculated by Ewald summation. The comparison is shown in Fig. 1(c), where the markers are the first-principles results and the solid lines are obtained using our model. It is clear that an excellent match is obtained in the low-energy part, which dominates the partition function relevant to the PE-FE phase transition.

## B. First-principles calculations

The DFT calculations were performed using the Vienna Ab initio Simulation Package (VASP) [23,24]. For electronic exchange and correlation interactions, the PBE+U functional is chosen [25,26]. The plane-wave cutoff energy is 500 eV. Concerning the Brillouin zone integration, we use a  $8 \times 8 \times 2$  **k**-grid.

The on-site Coulomb interaction parameters are specified with  $U = 5.0$  eV and  $J = 1.0$  eV [9]. Structural relaxation is performed with a conjugated-gradient algorithm, until the Hellmann-Feynman forces on each atom are less than  $0.1$  meV  $\text{\AA}^{-1}$ . The phonon spectrum and phonon eigenvectors are given by PHONOPY [27]. In Fig. 1, the PES curves at  $\Gamma$ ,  $M$ , and  $A$  are given by phonon calculations on a  $2 \times 2 \times 2$  supercell, while the curve at  $K$  is calculated using a  $3 \times 3 \times 1$  supercell.

### C. Path-integral Monte Carlo simulations

When the model Hamiltonian is constructed, we perform path-integral Monte Carlo (PIMC) to simulate the finite- $T$  polarization properties [28]. For  $\text{BaFe}_{12}\text{O}_{19}$ , our simulations were performed on a  $12 \times 12 \times 6$  supercell. For the PIMC simulation at each  $T$ , we performed 200 000 Monte-Carlo sweeps (MCS) for thermalization and 1 000 000 MCS for statistics. Concerning the number of time slices ( $N_{\text{time-slice}}$ ) for the path integral, we use  $TN_{\text{time-slice}} = 600$ , where  $T$  is the temperature in degrees Kelvin, and  $N_{\text{time-slice}}$  is the number of time slices, to keep a small enough Trotter error (the change of total energy is less than 0.02 meV/per site), and we use the bisection algorithm to improve the sampling efficiency [28]. The characteristic vibrational frequencies of the soft modes are small in both systems studied. Therefore, this parameter is sufficient for getting the PIMC simulation results converged with respect to the number of time slices.

## III. RESULTS

### A. DFT ground state

We first performed first-principles calculations to confirm the electric dipole configuration of the static ground-state crystal structure. Distorted crystal structures with different amplitudes along the soft phonon modes at the high-symmetry  $\mathbf{k}$ -points were created and we obtained their total energy by first-principles calculations. The total energies versus amplitudes along different soft modes were shown in Fig. 1(c) by square, circle, triangle, and star solid (hollow) markers, corresponding to the FE (AFE) soft modes at the high-symmetry  $\mathbf{k}$ -points  $\Gamma$ , M, K, and A. The minimal energy can be reached along the FE mode at M(0.5, 0, 0), which means that the DFT ground state of  $\text{BaFe}_{12}\text{O}_{19}$  is most likely a stripy AFE state with polarizations of the lattice Wannier functions on two 2b sites in a unit cell pointing to the same direction along the  $c$ -axis. This is consistent with previous theoretical calculations using first-principles calculations, as well as classical Monte Carlo simulations using a simpler model with classical dipole-dipole interactions [9].

In the meantime, we also noticed that many other modes, such as  $\Gamma$ -FE, M-AFE, K-FE, and K-AFE modes, have low-lying states on their PES with similar energies. Therefore, to make a good description of  $\text{BaFe}_{12}\text{O}_{19}$ 's complex PES, we need a method that is able to include more information of soft modes at different  $\mathbf{k}$ -points. This is also why the lattice Wannier function method is chosen.

### B. Dielectric constants

Now we include finite- $T$  statistical effects at two levels. Classical Monte Carlo (CMC) method includes classical statistical effects, and it corresponds to the  $N_{\text{time-slice}} = 1$  case of the PIMC method. When the PIMC simulations are converged with respect to  $N_{\text{time-slice}}$ , the quantum nuclear effects were also included. As such, comparisons of the CMC and PIMC results allow us to address the quantum nature of the nuclei in a very clean manner.

The  $T$ -dependent susceptibilities using the above effective lattice Hamiltonian with CMC and PIMC are shown in

Fig. 3(a). This susceptibility is defined as  $\chi = \frac{\beta N_{\text{site}}}{\epsilon_0 V} (\langle \bar{p}^2 \rangle - \langle \bar{p} \rangle^2)$ , where  $V$  denotes the unit-cell volume,  $\epsilon_0$  means the vacuum dielectric constant,  $\beta$  is the inverse temperature,  $\bar{p} = \frac{1}{N_{\text{site}} N_{\text{time-slice}}} \sum_{\tau} \sum_i^{N_{\text{site}}} p_i^{\tau}$  denotes the averaged on-site dipole moments over the sites and the time slices of imaginary-time path-integral, and  $\langle \dots \rangle$  represents the ensemble average [29]. Due to the imperfection of the DFT PES, we add a small strain, which stretches the length of the  $c$ -axis about 0.15%, for a better fitting of the dielectric constants obtained by our simulations to experiments [30]. The susceptibility given by CMC shows a peak at 10 K. In the higher- $T$  region, the susceptibility shows a Curie-Weiss-like behavior, which means that  $\text{BaFe}_{12}\text{O}_{19}$  is in a PE state.

The inverse of the susceptibility from the CMC simulations was shown in Fig. 3(b), together with a linear fitting denoted by the red dashed line. The absolute value of linear extrapolated  $T_C$  is  $\sim 25$  K, with the negative sign representing a signature of the AFE coupling. In the lower- $T$  region, the susceptibility drops off. This means that the system is frozen in a minimum of the PES upon cooling, so that the polarization is hardly changed by an external electric field. We note, however, that such a behavior has not been observed in experiments.

Rather, a plateau of dielectric constant (susceptibility) appears at low  $T$  [10,11], as a signal of the QPE. Therefore, we move on to perform PIMC simulations to address the quantum fluctuations of the nuclei.

Our PIMC simulations accurately reproduced the low- $T$  plateau of the susceptibility, as shown in Fig. 3(a), where the experimental results are black squares and the PIMC results are purple circles (zoom-in in the inset). This qualitative difference between the CMC and PIMC results and the nice agreement between the latter and the experimental values unambiguously mean that the experimentally observed plateau is due to the quantum fluctuations of the nuclei, i.e.,  $\text{BaFe}_{12}\text{O}_{19}$  is QPE. Then we fit our results by the Barrett formula [31] (red dashed line),

$$\chi = A + \frac{M}{0.5T_1 \coth\left(\frac{T_1}{2T}\right) - T_0}, \quad (3)$$

which has been proven to give a good description of the QPE of the perovskites [4,31].

In this equation,  $A$  and  $M$  are constants,  $T_0$  reflects the strength of intersite coupling, and  $T_1$ , when quantum fluctuations dominate, represents the tunneling strength. After fitting, we obtained  $T_0 \approx -11.31$  K and  $T_1 \approx 13.42$  K, which are qualitatively consistent with a previous experiment that yielded  $T_0 = -22.9$  K and  $T_1 = 47.3$  K [11].

For a more in-depth understanding of the QPE nature of the low- $T$  plateau, we further decompose the contributions from the thermal and quantum fluctuations of the nuclei at varying  $T$ 's using a method proposed by Zhong and Vanderbilt in Ref. [3]. The thermal fluctuation is defined as  $\Delta u_{\text{thermal}}^2 = \langle (u_s^2)_{i,t} \rangle$ , where  $s$  denotes the time slice in the PIMC simulations,  $i$  denotes the lattice site, and  $t$  denotes the Monte Carlo sweep.

In the language of a path integral, the centroid positions often refer to a classical analogy of the quantum paths, and these two quantities become exactly the same at high  $T$ . The

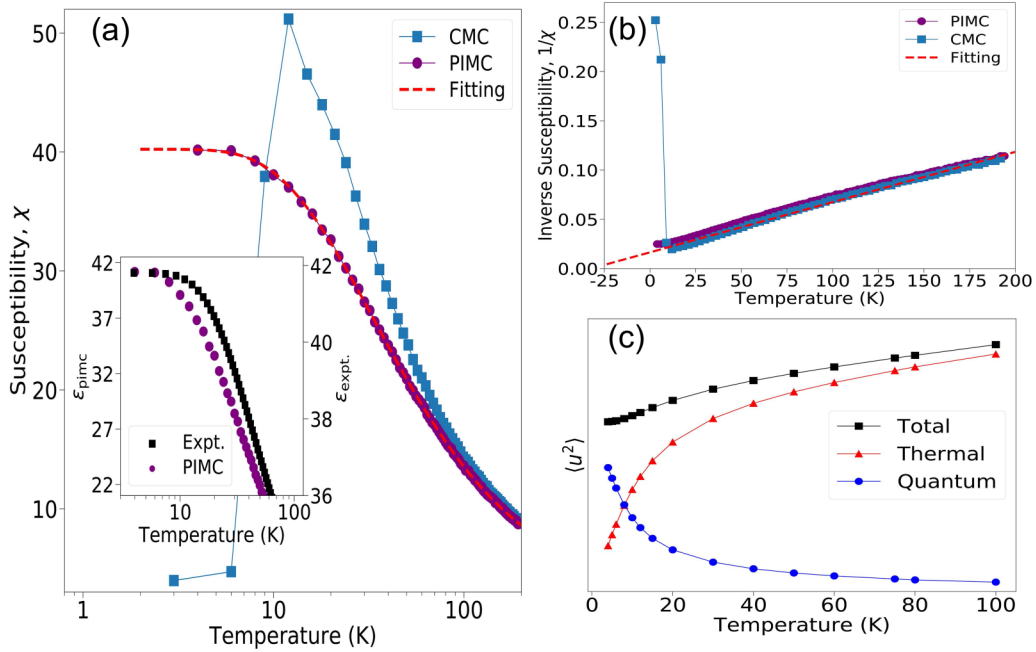


FIG. 3. (a) Susceptibility vs temperature calculated by CMC and PIMC simulations with strain along the  $c$ -axis,  $\eta_c = 0.15\%$ . The red dashed line is fitted by the Barrett formula. Inset of (a): Compare between PIMC results (purple circles) and previous experiments (black dots); the experimental data are extracted from Shen *et al.*'s paper [11]. (b) The inverse of the susceptibility from CMC (blue squares), PIMC (purple circles), and a linear fitting to the CMC results (dashed line). (c) The thermal and quantum contribution to the fluctuations vs  $T$ .

total fluctuation is  $\Delta u_{\text{total}}^2 = \langle u^2 \rangle_{i,s,t}$ . With these two quantities, a crude estimation of the quantum contribution to the nuclear fluctuations can be given by  $\Delta u_{\text{total}}^2 - \Delta u_{\text{thermal}}^2$ . The numerical results are shown in Fig. 3(c).

The proportion of quantum contributions decreases gradually with the increase of  $T$  until the region when thermal contributions are dominant, which corresponds to the classical paraelectric phase as appeared in the conventional Curie-Weiss theory. At low  $T$ , the quantum contribution crosses over with the classical one at  $\sim 10$  K, below which the quantum fluctuation is dominant. It is responsible for the plateau of susceptibility as observed in the experiments. Therefore, the picture that the low- $T$  behaviors of susceptibility originate from the quantum fluctuations of the nuclei is further confirmed.

### C. The influence of geometrical frustration

Due to the triangular lattice and AFE-type nearest-neighbor intersite coupling of BaFe<sub>12</sub>O<sub>19</sub>, the influence of geometrical frustration on the experimental observations of the dielectric function is worthy of further study. For a system with geometrical frustration, there is a large number of low-energy dipole configurations having the same energy, so that the system cannot reach an ordered state and become paraelectric. Therefore, if the paraelectric behaviors were due to the geometrical frustration, it will be easily broken when the geometrical frustration is broken. To test this, we change the nearest-neighbor coupling  $J_1$  of the short-range term on one of the three bonds of the triangular lattice. The calculated susceptibility was shown in Fig. 4. The results denoted by square and triangular markers correspond to the case when we choose  $J_1' = 0.5J_1$  and  $1.5J_1$ , respectively. The circles denote

the results when  $J_1$  is not changed so that the symmetry and geometry frustration are preserved.

When the symmetry is broken, the susceptibility changes little and still shows a low- $T$  plateau, meaning that this plateau is irrelevant to geometry frustrations. Rather, the qualitative difference between the CMC and PIMC results as shown in Fig. 3(a) is the reason for the nontrivial electric polarization behaviors as observed in the experiments [11].

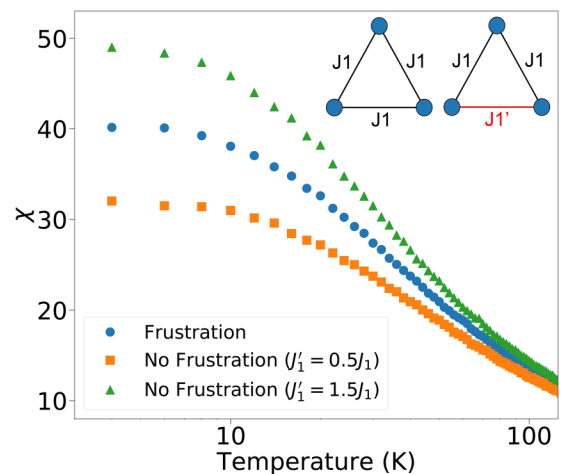


FIG. 4. Susceptibility with changed nearest-neighbor short-range intersite coupling  $J_1$ . The circles denote that  $J_1$  is not changed so that the symmetry and geometry frustration are preserved. To compare, one can also change one  $J_1$  of the three bonds of the triangular lattice, as schematically shown on the upper right corner. The red line denotes the changed bonds. Squares denote the results when  $J_1' = 0.5J_1$  and triangles denote the results when  $J_1' = 1.5J_1$ .

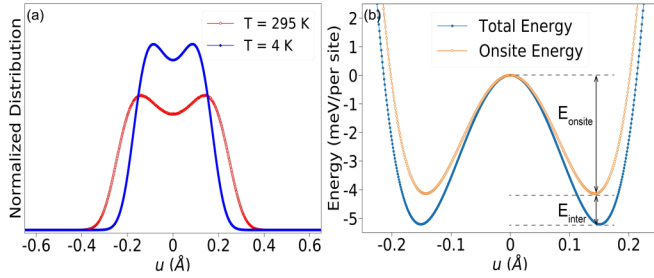


FIG. 5. (a) Distributions of the amplitude  $u$  of the lattice Wannier functions at 4 and 295 K. (b)  $u$ -dependence of the total and on-site energies with M-FE dipole configuration.

#### D. Order-disorder/displacive behaviors

As we have mentioned above, many experiments on the crystal structure of  $\text{BaFe}_{12}\text{O}_{19}$  have observed the displacements of Fe ions at the Fe-O TBP site. To understand this, we plot the distributions of the amplitude of our lattice Wannier function at 4 and 295 K, denoted as  $u$ , along the  $c$  axis in Fig. 5(a). According to our construction of the lattice Wannier function, the displacement of the Fe ion on the 2b site roughly equals  $0.96u$ .

From this relation, we estimate that the Fe-Fe distance obtained by our simulations is  $0.164 \text{ \AA}$  at 4 K ( $0.267 \text{ \AA}$  at 295 K). It represents a good agreement with the experimental results, e.g., in a recent neutron diffraction experiment [8], the Fe-Fe distance is  $0.196$  and  $0.354 \text{ \AA}$  at 4 and 295 K, respectively.

Thus, the experimental observations can be understood as having the Fe ions on the Fe-O TBP sites being “split” into two half ions from the mirror plane of TBP [15], by statistical average. This double-peak distribution implies an order-disorder nature of the paraelectrics, meaning that the long-range order is erased by fluctuations, but the local electric dipoles (distortion of crystal structure) persist. For a conventional FE-PE phase transition induced by thermal fluctuations, one can classify paraelectric properties as displacive or order-disorder-type according to the microscopic behaviors when the FE materials become PE upon heating.

In the QPEs, whether displacive or order-disorder nature dominates the paraelectric properties can be determined by the relationship between the on-site energy  $E_{\text{on-site}}$ , the inter-site coupling  $E_{\text{inter}}$ , and the quantum fluctuations  $Q$ , as we shown in Table I. The on-site energy,  $E_{\text{on-site}}$ , is the static energy

TABLE I. Displacive or order-disorder behaviors determined by the relationship between and among  $E_{\text{on-site}}$ ,  $E_{\text{inter}}$ , and the quantum fluctuations  $Q$ .

$E_{\text{on-site}} > E_{\text{inter}}$		
	$Q > E_{\text{on-site}}$	Displacive QPE
	$E_{\text{on-site}} > Q > E_{\text{inter}}$	Order-disorder QPE
	$Q < E_{\text{inter}}$	FE
$E_{\text{on-site}} < E_{\text{inter}}$		
	$Q > E_{\text{inter}}$	Displacive QPE
	$Q < E_{\text{inter}}$	FE

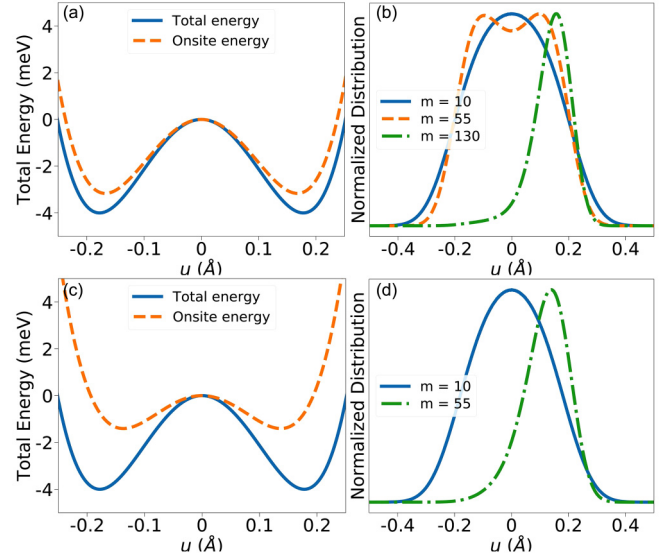


FIG. 6. Parts (a) and (c) show the  $u$ -dependence of the total and on-site energies for the case of  $E_{\text{on-site}} > E_{\text{inter}}$  and  $E_{\text{on-site}} < E_{\text{inter}}$ , respectively. Parts (b) and (d) show the distributions of  $u$  obtained by performing PIMC simulations (4 K with  $TN_{\text{time-slice}} = 600$ ) for systems shown in (a) and (c), respectively, with different effective mass. In panel (b), the effective mass  $m = 10, 55$ , and  $130$  corresponds to the case of displacive QPE, order-disorder QPE, and ordered FE, respectively. In panel (d), the effective mass  $m = 10$  and  $55$  corresponds to the case of displacive QPE and ordered FE. We renormalize the maxima of all distributions to the same value for clarity.

reduction when a local structural distortion (local electric dipole) arises from the high-symmetry crystal structure. The intersite energy,  $E_{\text{inter}}$ , is the further energy reduction when the local electric dipoles form a long-range ordered state by the inter-site coupling. The quantum fluctuations  $Q$  can be treated as a constant for a given system at low  $T$ , differing from the thermal fluctuations which vanish upon cooling.

When  $E_{\text{on-site}} > Q > E_{\text{inter}}$ , fluctuations can easily suppress the long-range order (whose formation is due to the intersite coupling) but cannot suppress the local electric dipoles (due to the on-site energy), so that the QPEs show order-disorder behavior. Conversely, when  $Q > E_{\text{on-site}}$  and  $Q > E_{\text{inter}}$ , the QPEs show a displacive nature since all the distortions are washed out by the large quantum fluctuations. If  $Q < E_{\text{inter}}$ , the quantum fluctuations cannot suppress the long-range order, so that the system will become FE at low  $T$ .

In  $\text{BaFe}_{12}\text{O}_{19}$ ,  $E_{\text{on-site}}$  and  $E_{\text{inter}}$  can be estimated by the on-site and intersite part of our effective Hamiltonian, respectively. The results are shown in Fig. 5(b), with  $E_{\text{on-site}} \approx 4.1 \text{ meV}$  and  $E_{\text{inter}} \approx 1.1 \text{ meV}$ .  $E_{\text{on-site}}$  is larger than  $E_{\text{inter}}$ , and the quantum fluctuation is not large enough to wash out the local moment, as shown in Fig. 5(a). Therefore, the QPE is clearly of an order-disorder-type nature.

To further confirm the conclusion shown in Table I, we design a simple model on a triangular lattice that only has the nearest-neighbor ( $J_1$ ) FE coupling. By changing the on-site quadratic coefficient, we can construct systems that satisfy  $E_{\text{on-site}} > E_{\text{inter}}$  or  $E_{\text{on-site}} < E_{\text{inter}}$  [the PES shown in Figs. 6(a)

and 6(c), respectively]. The influence of quantum fluctuations on these systems was simulated by PIMC, and the strength of quantum fluctuations is tuned by changing the magnitude of the effective mass (smaller mass gives larger quantum fluctuations).

The distributions corresponding to different cases are shown in Fig. 6(b) ( $E_{\text{on-site}} > E_{\text{inter}}$  case) and Fig. 6(d) ( $E_{\text{on-site}} < E_{\text{inter}}$  case). These results show good agreement with the conclusion in Table I. Therefore, we suggest that Table I can be used as a simple rule of thumb to distinguish different local behaviors of the electric dipoles in QPEs.

#### IV. CONCLUSION

In summary, we performed PIMC simulations combined with an accuracy effective lattice Hamiltonian in terms of the lattice Wannier function to study the electric polarization behaviors of BaFe<sub>12</sub>O<sub>19</sub>. The quantum paraelectricity nature of BaFe<sub>12</sub>O<sub>19</sub> is confirmed, which shows a clear plateau of dielectric constants and large quantum contribution of fluctuations at low  $T$ . By constructing an artificial system in which geometry frustration is broken, we found that the geometry frustration plays an unimportant role in the QPE behavior of BaFe<sub>12</sub>O<sub>19</sub>. Finally, we show that QPE can have

order-disorder or displacive natures, such as what exists in the thermal paraelectrics. This classification can be understood using a very simple descriptor, i.e., the relative magnitude of the on-site, intersite energies of electric dipoles, and quantum fluctuations. The QPE in BaFe<sub>12</sub>O<sub>19</sub> is of an order-disorder nature.

These results show good agreement with the previous experiments of a crystal structure. It should be noted that the order parameter of BaFe<sub>12</sub>O<sub>19</sub>, which is a scalar, is different from that of the perovskites (e.g., SrTiO<sub>3</sub>), which is a three-component vector. All these characters give persuasive evidence of a new type of QPE, which is different from the well-known QPE, SrTiO<sub>3</sub>. We hope that these results will enrich our theoretical understanding of QPEs.

#### ACKNOWLEDGMENTS

The authors are supported by the National Basic Research Programs of China under Grant No. 2016YFA0300900, and the National Science Foundation of China under Grants No. 11774003, No. 11825403, No. 11934003, and No. 11634001. They are grateful for the stimulating discussions with Y. S. Chai. The computational resources were provided by the supercomputer center in Peking University, China.

- 
- [1] R. Roussev and A. J. Millis, *Phys. Rev. B* **67**, 014105 (2003).
  - [2] K. A. Müller and H. Burkard, *Phys. Rev. B* **19**, 3593 (1979).
  - [3] W. Zhong and D. Vanderbilt, *Phys. Rev. B* **53**, 5047 (1996).
  - [4] A. R. Akbarzadeh, L. Bellaïche, K. Leung, J. Íñiguez, and D. Vanderbilt, *Phys. Rev. B* **70**, 054103 (2004).
  - [5] G. J. Conduit and B. D. Simons, *Phys. Rev. B* **81**, 024102 (2010).
  - [6] S. E. Rowley, L. J. Spalek, R. P. Smith, M. P. M. Dean, M. Itoh, J. F. Scott, G. G. Lonzarich, and S. S. Saxena, *Nat. Phys.* **10**, 367 (2014).
  - [7] R. C. Pullar, *Prog. Mater. Sci.* **57**, 1191 (2012).
  - [8] H. B. Cao, Z. Y. Zhao, M. Lee, E. S. Choi, M. A. McGuire, B. C. Sales, H. D. Zhou, J.-Q. Yan, and D. G. Mandrus, *APL Mater.* **3**, 062512 (2015).
  - [9] P. S. Wang and H. J. Xiang, *Phys. Rev. X* **4**, 011035 (2014).
  - [10] S.-P. Shen, Y.-S. Chai, J.-Z. Cong, P.-J. Sun, J. Lu, L.-Q. Yan, S.-G. Wang, and Y. Sun, *Phys. Rev. B* **90**, 180404(R) (2014).
  - [11] S.-P. Shen, J.-C. Wu, J.-D. Song, X.-F. Sun, Y.-F. Yang, Y.-S. Chai, D.-S. Shang, S.-G. Wang, J. F. Scott, and Y. Sun, *Nat. Commun.* **7**, 10569 (2016).
  - [12] E. F. Bertaut, A. Deschamps, R. Pauthenet, and S. Pickart, *J. Phys. Radium* **20**, 404 (1959).
  - [13] J. Rensen and J. van Wieringen, *Solid State Commun.* **7**, 1139 (1969).
  - [14] G. Albanese, A. Deriu, and D. Cabrini, *Hyperfine Interact.* **70**, 1087 (1992).
  - [15] W. D. Townes, J. H. Fang, and A. J. Perrotta, *Z. Krist.* **125**, 437 (1967).
  - [16] A. Collomb, P. Wolfers, and X. Obradors, *J. Magn. Magn. Mater.* **62**, 57 (1986).
  - [17] J. Íñiguez, A. García, and J. M. Pérez-Mato, *Phys. Rev. B* **61**, 3127 (2000).
  - [18] T. Schneider, H. Beck, and E. Stoll, *Phys. Rev. B* **13**, 1123 (1976).
  - [19] W. Kohn, *Phys. Rev. B* **7**, 2285 (1973).
  - [20] N. Marzari, A. A. Mostofi, J. R. Yates, I. Souza, and D. Vanderbilt, *Rev. Mod. Phys.* **84**, 1419 (2012).
  - [21] K. M. Rabe and U. V. Waghmare, *Phys. Rev. B* **52**, 13236 (1995).
  - [22] F. Giustino and A. Pasquarello, *Phys. Rev. Lett.* **96**, 216403 (2006).
  - [23] G. Kresse and J. Furthmüller, *Phys. Rev. B* **54**, 11169 (1996).
  - [24] G. Kresse and J. Furthmüller, *Comput. Mater. Sci.* **6**, 15 (1996).
  - [25] J. P. Perdew, K. Burke, and M. Ernzerhof, *Phys. Rev. Lett.* **77**, 3865 (1996).
  - [26] A. I. Liechtenstein, V. I. Anisimov, and J. Zaanen, *Phys. Rev. B* **52**, R5467 (1995).
  - [27] A. Togo and I. Tanaka, *Scr. Mater.* **108**, 1 (2015).
  - [28] D. M. Ceperley, *Rev. Mod. Phys.* **67**, 279 (1995).
  - [29] A. García and D. Vanderbilt, in *The 5th Williamsburg Workshop on First-Principles Calculations for Ferroelectrics*, edited by R. Cohen, Vol. 436 (Williamsburg, VA, 1998), p. 53.
  - [30] W. Zhong, D. Vanderbilt, and K. M. Rabe, *Phys. Rev. B* **52**, 6301 (1995).
  - [31] J. H. Barrett, *Phys. Rev.* **86**, 118 (1952).